Large spin-orbit torque observed in epitaxial SrIrO 3 thin films

Applied Physics Letters

Large spin-orbit torque observed in epitaxial $SrIrO_3$ thin films

Cite as: Appl. Phys. Lett. **114**, 232406 (2019); https://doi.org/10.1063/1.5097699
Submitted: 27 March 2019 . Accepted: 31 May 2019 . Published Online: 13 June 2019

Hailong Wang, Keng-Yuan Meng, Pengxiang Zhang, Justin T. Hou, Joseph Finley, Jiahao Han, Fengyuan Yang, and Luqiao Liu

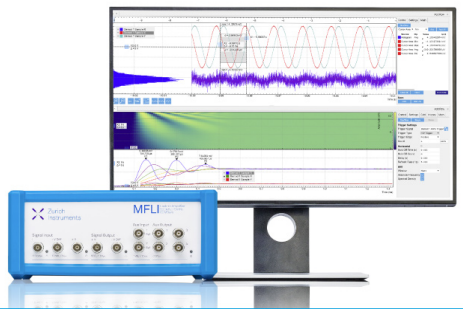

Applied Physics Letters ARTICLE scitation.org/journal/apl

Large spin-orbit torque observed in epitaxial $SrIrO_3$ thin films

Cite as: Appl. Phys. Lett. **114**, 232406 (2019); doi: 10.1063/1.5097699
Submitted: 27 March 2019 · Accepted: 31 May 2019 ·
Published Online: 13 June 2019

Hailong Wang,[1,a),b)] Keng-Yuan Meng,[2] Pengxiang Zhang,[1] Justin T. Hou,[1] Joseph Finley,[1] Jiahao Han,[1] Fengyuan Yang,[2] and Luqiao Liu[1,b)]

AFFILIATIONS

[1]Department of Electrical Engineering and Computer Science, Massachusetts Institute of Technology, Cambridge, Massachusetts 02139, USA
[2]Department of Physics, The Ohio State University, Columbus, Ohio 43210, USA

[a)]**Current address:** Center for Memory and Recording Research, University of California, San Diego, La Jolla, CA 92093, USA.
[b)]**Authors to whom correspondence should be addressed:** hailongwang1988@gmail.com and luqiao@mit.edu

ABSTRACT

Semimetallic iridate compound $SrIrO_3$ epitaxial films have been deposited by off-axis sputtering, exhibiting excellent crystalline quality as well as smooth surfaces. By performing second-harmonic Hall measurements on a series of $SrIrO_3/Co_{1-x}Tb_x$ bilayers, we quantitatively determined the spin-to-charge interconversion efficiency θ_{SH} of $SrIrO_3$ and discovered a systematic temperature and film thickness dependent evolution behavior. Notably, the measured $|\theta_{SH}|$ reaches a remarkably large number of $\sim$1.1 at room temperature, which is significantly larger than the value of 5*d* transition metals and comparable to the values reported in some topological material systems. Our findings are further corroborated by ferromagnetic resonance-driven spin pumping studies in $SrIrO_3$/Py bilayers, highlighting the significant opportunities offered by the iridate compounds in designing next-generation energy-efficient multifunctional spin Hall devices.

Spin–orbit coupling (SOC) plays a central role in modern spintronic research[1–7] and for the formation of many exotic quantum phases recently discovered in condensed matter physics such as topological insulators,[8] Weyl semimetals,[9] and quantum spin Hall insulators.[10] The iridate compounds, a group of 5*d* transition metal oxides, are naturally relevant to this context due to the heavy element iridium (atomic number $z = 77$), which tends to exhibit large SOC.[11–14] Additionally, the intrinsic sensitivities of complex oxide thin films to the oxygen deficiency, epitaxial strain, film thickness, and stoichiometry provide multiple tuning knobs to efficiently control the electronic and magnetic properties and the associated SOC,[15–19] promising to bring in desirable functionality for the design of next-generation spintronic devices. To realize these potential benefits, single crystalline oxide thin films with delicately controlled material properties are needed, which require cutting-edge deposition techniques that involve fine tuning of oxygen content, layer-by-layer growth scheme, and accurate control of the epitaxial strain and relaxation. In this work, we have achieved the growth of ferrimagnetic Co_xTb_{1-x} alloy thin films with perpendicular magnetic anisotropy (PMA) onto single crystalline $SrIrO_3$ epitaxial films. With the bilayer structure, we determine the spin-to-charge interconversion ratio, the figure of merit for spintronic application, of $SrIrO_3$ to be as large as 1.1. The demonstrated large spin-to-charge interconversion efficiency points to the possibility of achieving devices with ultralow power consumption for magnetic memory and spin logic by incorporating complex oxides into the material landscape of spintronic research.

We first discuss the structural and interfacial condition of the prepared $SrIrO_3$ thin films. Epitaxial $SrIrO_3$ films are deposited on (001)-oriented $SrTiO_3$ substrates using the off-axis sputtering technique.[15,16] The crystalline quality of the $SrIrO_3$ films is determined by high-resolution X-ray diffraction (XRD). A representative θ-2θ scan with 2θ between 15° and 55° is shown in Fig. 1(a), which indicates the phase-pure epitaxial growth of a 30-nm thick $SrIrO_3$ film. A zoom-in view of the (002) peak in the inset exhibits pronounced Laue oscillations, reflecting a smooth surface and sharp $SrIrO_3/SrTiO_3$ interface. We find an out-of-plane lattice constant of the $SrIrO_3$ film, $c = 4.053$ Å, larger than the bulk value of 3.942 Å, suggesting a compressive strain induced by the $SrTiO_3$ substrate. Figure 1(b) shows the X-ray reflectometry (XRR) spectrum of a 30-nm thick $SrIrO_3$, exhibiting a clear oscillation period from which the film thickness can be accurately determined. The atomic force microscopy (AFM) image of

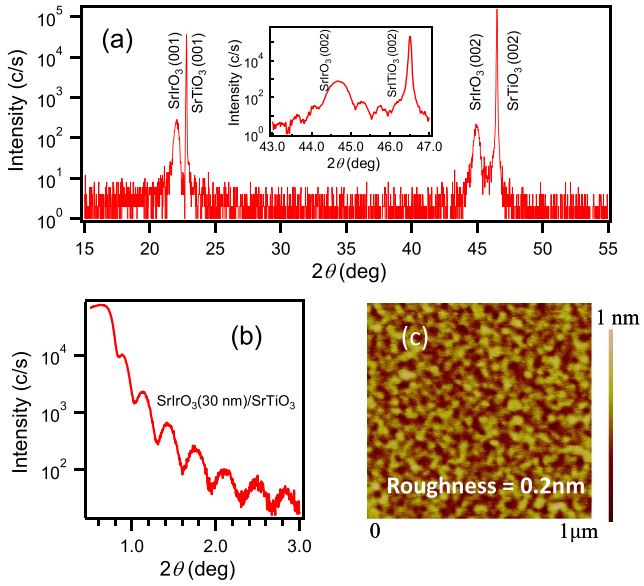

FIG. 1. (a) Wide angle semilog θ-2θ XRD scan of a 30-nm thick $SrIrO_3$ film grown on a $SrTiO_3$ (001) substrate. Inset: zoom-in view of the (002) peak exhibits pronounced Laue oscillations. (b) XRR scan of a $SrIrO_3$ film shows a clear oscillation period, corresponding to the film thickness. (c) AFM image of a $SrIrO_3$ film with a rms roughness of 0.2 nm.

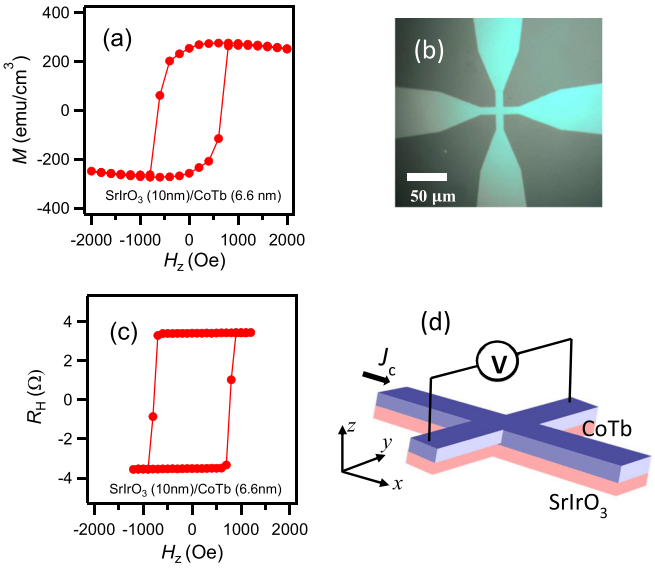

FIG. 2. (a) Room temperature out-of-plane magnetic hysteresis loop of a $SrIrO_3$(10 nm)/CoTb(6.6 nm) sample measured by vibrating sample magnetometry. (b) Image of a patterned $SrIrO_3$(10 nm)/CoTb(6.6 nm) Hall bar device with a channel width of 10 μ m. (c) The measured anomalous Hall resistance R_H of a $SrIrO_3$(10 nm)/CoTb(6.6 nm) Hall bar device as a function of out-of-plane magnetic field H_z. (d) Schematic of a Hall bar device with an illustration of the performed harmonic Hall measurement scheme. The AC current is applied along the x-axis and the anomalous Hall voltage is detected along the y-axis.

the same sample shown in Fig. 1(c) gives a root mean square (rms) roughness of ~0.2 nm.

The first experimental approach that we employ to calibrate the spin-to-charge conversion of epitaxial $SrIrO_3$ thin films is the second-harmonic Hall measurement.[20–24] This method has been widely used in a variety of magnetic heterostructures consisting of heavy metals and perpendicularly magnetized ferromagnets. Here, we choose ferrimagnetic $Co_{1-x}Tb_x$ (CoTb) alloy with strong PMA[25–29] as the magnetic electrode and deposit 6.6-nm thick $Co_{1-x}Tb_x$ onto a series of $SrIrO_3$ thin films with different thicknesses. The deposition of the $Co_{1-x}Tb_x$ film is followed by a 3-nm thick SiN_x capping layer to prevent oxidization of this magnetic layer. A vibrating-sample magnetometry (VSM) measurement is carried out on the samples with the field applied along the out-of-plane direction. The result shown in Fig. 2(a) clearly demonstrates the PMA of the $Co_{1-x}Tb_x$ film on $SrIrO_3$. In our experiment, $Co_{1-x}Tb_x$ (CoTb) with different chemical compositions is tested. We conclude that a Tb atomic ratio of $x = 0.23$ is optimal for achieving a square magnetic hysteresis loop. In order to perform harmonic Hall measurements, the continuous thin films are patterned into micrometer-sized Hall bar structures by standard photolithography and dry etching processes with a channel width of 10 μm [Fig. 2(b)]. Figure 2(c) shows the measured anomalous Hall resistance R_H of a fabricated device as a function of out-of-plane magnetic field H_z. The measured hysteresis loop follows a similar behavior of the VSM results and the coercivity is determined to be ~800 Oe. The resistivities of the $SrIrO_3$ and CoTb films are separately determined to be $1.2 \times 10^{-5}\,\Omega$ m and $1.0 \times 10^{-5}\,\Omega$ m, respectively. We note that the resistivity of $SrIrO_3$ exhibits a weak dependence on the thin film thickness in the regime that we studied. A parallel circuit model is used in the analysis of current distribution in the rest of the discussions.

We use the experimental geometry shown in Fig. 2(d) for quantifying the spin Hall effect in $SrIrO_3$. When an electric charge current J_c flows through the $SrIrO_3$ layer along the x-axis, a spin current will be generated along the z-axis with spin polarization $\boldsymbol{\sigma}$ oriented along the y-axis by the spin Hall effect. The accumulated spin current J_s is injected into the CoTb magnetic free layer, inducing a dampinglike torque $\tau_{DL} \sim \boldsymbol{m} \times (\boldsymbol{\sigma} \times \boldsymbol{m})$ and a fieldlike torque $\tau_{FL} \sim \boldsymbol{\sigma} \times \boldsymbol{m}$,[30] where $\boldsymbol{m}$ denotes the magnetization of the CoTb layer. When the magnetic moment reaches an equilibrium position, the effects of these two torques can also be described equivalently through the generated longitudinal $\Delta H_L \sim \boldsymbol{m} \times \boldsymbol{\sigma}$ and transverse effective fields $\Delta H_T \sim \boldsymbol{\sigma}$, respectively. When an alternating current (AC) is applied through the device channel, the generated $\Delta H_{L(T)}$ causes an oscillation of the CoTb magnetization $\boldsymbol{m}$ around the equilibrium position. By sweeping an in-plane external field parallel (H_L, along the $\pm x$-axis) and transverse (H_T, along the $\pm y$-axis) to the current flow direction, we can measure the field dependence of the first-harmonic signal V_ω and the out-of-phased (90° off) second-harmonic signal $V_{2\omega}$, from which $\Delta H_{L(T)}$ can be extracted using[21]

$$\Delta H_{L(T)} = -2\frac{dV_{2\omega}/dH_{L(T)}}{d^2V_\omega/dH_{L(T)}^2}. \quad (1)$$

Figures 3(a) and 3(b) show the in-plane field (H_L) dependence of the measured first-harmonic (V_ω) and second-harmonic ($V_{2\omega}$) signals, respectively, of a $SrIrO_3$(10 nm)/CoTb(6.6 nm) Hall device. It is noted that V_ω exhibits a characteristic parabolic behavior with opposite polarities for magnetization pointing along $+z$ and $-z$ directions,

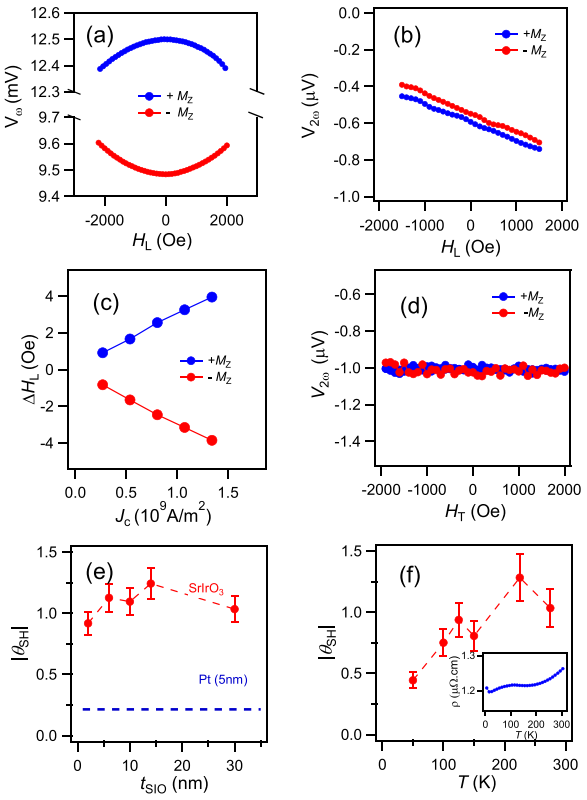

FIG. 3. In-plane longitudinal field H_L dependence of the measured (a) first-harmonic Hall signal V_ω and (b) second-harmonic Hall signal $V_{2\omega}$ of a $SrIrO_3$(10 nm)/CoTb(6.6 nm) Hall device. (c) The measured effective field ΔH_L along the longitudinal direction as a function of the applied electrical current density J_c flowing through the $SrIrO_3$ layer. (d) In-plane transverse field H_T dependence of the measured second-harmonic Hall signal $V_{2\omega}$. Blue and red curves represent signals when the magnetization points along the $+z$ and $-z$ directions, respectively. (e) $SrIrO_3$ film thickness t_{SIO} dependence of the obtained θ_{SH}. The blue dashed line indicates the obtained θ_{SH} for Pt through the same harmonic Hall measurements in a Pt/CoTb control sample. (f) Temperature dependence of θ_{SH} measured in the $SrIrO_3$(30 nm)/CoTb(6.6 nm) Hall device in the range of 50–300 K. Inset: temperature dependent resistivity ρ of a 10-nm $SrIrO_3$ thin film.

while $V_{2\omega}$ follows a linear dependence on H_L and the slopes are the same for both magnetic states, which are consistent with the origin of the spin Hall effect induced dampinglike torque.[21,29] Using Eq. (1), we calculate ΔH_L under different J_c and summarize the results in Fig. 3(c). Remarkably, a robust $\Delta H_L \sim 4$ Oe was generated at a fairly low electrical current density down to 1.3×10^9 A/m^2, suggesting an extraordinarily large SOC of the epitaxial $SrIrO_3$ film. We note that ΔH_L linearly increases with the magnitude of J_c and switches the sign when $\boldsymbol{m}$ flips from the $+z$ to $-z$ direction. Here, we can exclude the contribution from the planar Hall effect and anomalous Nernst effect due to the relatively small field range compared with the strong PMA of the CoTb thin film.[20] With equation $\theta_{SH} = \frac{2e\mu_0 M_s \Delta H_L t_{CoTb}}{J_c \hbar}$,[31] $|\theta_{SH}|$ is determined to be 1.08 ± 0.11, significantly larger than the value of 0.22 ± 0.02 of the Pt layer measured in a Pt/CoTb control sample. Here, e is the electron charge, μ_0 is the vacuum permeability, $\hbar$ is the reduced Planck's constant, M_s is the saturated magnetization, and t_{CoTb} is the thickness of the CoTb layer. It is noted that the measured $V_{2\omega}$ of the same device exhibits little dependence on H_T as shown in Fig. 3(d), indicating a negligible contribution from the fieldlike torque generated by the spin Hall effect of the $SrIrO_3$ layer.

For complex oxide thin films, it is known that the exhibited properties are intrinsically sensitive to strain-induced structural distortions, which is strongly correlated with the film thickness. To explore this possibility, we systematically varied the film thickness of $SrIrO_3$ from 2 to 30 nm to reveal the evolution of θ_{SH}. As shown in Fig. 3(e), the obtained $|\theta_{SH}|$ remains mostly constant around 0.8–1.2 in the whole thickness range. A possible explanation on the absence of thickness dependence is that the measured spin–orbit torque efficiency heavily depends on the $SrIrO_3$/CoTb interface, which exhibits a reduced sensitivity to the substrate-induced epitaxial strain and lattice distortions. Here, we do not observe the crystallographic-oriented dependence of the spin Hall angle as reported in Ref. 14. Besides the thickness dependence, we also carried out experiments to measure $|\theta_{SH}|$ at different temperatures. The results for a 30-nm thick $SrIrO_3$ sample are shown in Fig. 3(f) with temperature varying between 50 K and 300 K. Across the temperature range, the value of $|\theta_{SH}|$ shows an increase from 0.44 ± 0.06 to 1.04 ± 0.15 and the saturation magnetization M_s exhibits a weak temperature dependence. Here, we note that the increase in the spin Hall conductivity with temperature indicates that the intrinsic effect cannot be the dominant mechanism.[32] A thorough understanding of this origin and the characteristic temperature dependence requires further systematic study which is beyond the scope of this manuscript.

The large spin–orbit torque measured in $SrIrO_3$ thin films suggests very efficient spin-to-charge interconversion, providing a promising material platform for energy-favorable spin generation and detection. Here, we utilized ferromagnetic resonance (FMR)-driven spin pumping,[33–36] a widely used experimental tool for detecting spin injections, as an alternative method to qualitatively calibrate θ_{SH} of $SrIrO_3$ films. Our spin pumping measurements were performed using a coplanar waveguide at room temperature on $SrIrO_3$/Py bilayers with an approximate sample dimension of 1 mm × 4 mm. During the measurements, a DC magnetic field H is applied along the x-axis and the generated spin pumping voltage V_{SP} is measured across the ~4-mm-long sample along the y-axis as illustrated in Fig. 4(a). At the FMR condition, the Py magnetization $\boldsymbol{M}$ precesses around the equilibrium position and transfers angular momentum to the conduction electrons in the neighboring $SrIrO_3$ layer through the interfacial exchange coupling,[37] resulting in pure spin current J_s along the z-axis with spin polarization σ parallel to $\boldsymbol{M}$. The injected spin current is converted to a charge current, $J_c \propto \theta_{SH}\, J_s \times \sigma$, by the inverse spin Hall effect (ISHE).[33]

The field dependent spin pumping signal from a $SrIrO_3$(10 nm)/Py(20 nm) sample is shown in Fig. 4(b) at frequency $f = 5.5$ GHz with microwave power $P_{rf} = 90$ mW at the sample location. The observed V_{SP} changes its sign when the external field H reverses the polarity, in consistent with the ISHE mechanism.[33] To compare the efficiency of spin-to-charge conversion in the $SrIrO_3$ sample with other well-studied materials, we employed a bilayer film of Pt(5 nm)/Py(20 nm) as a control sample. Notably, the measured V_{SP} of the $SrIrO_3$/Py sample exhibits an opposite sign compared with the signal of the Pt/Py bilayer, indicating a negative θ_{SH} of $SrIrO_3$, in agreement with our harmonic Hall measurement results. The observed spin pumping spectra are dominated by a symmetric Lorenz shape, suggesting a negligible

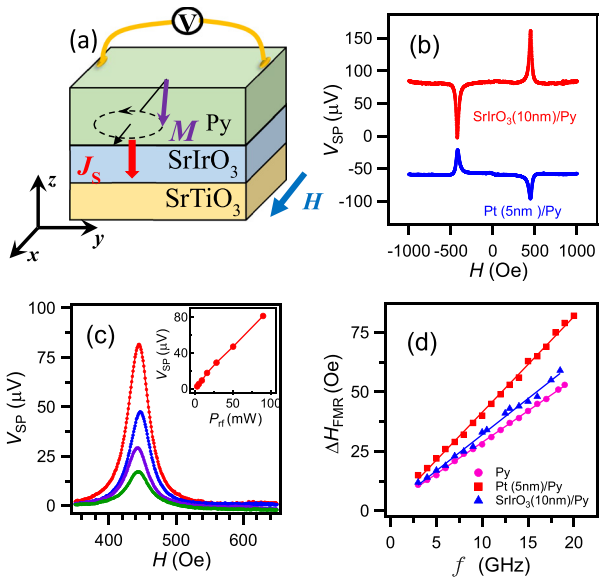

FIG. 4. (a) Schematic diagram of the ISHE voltage measurement setup. (b) V_{SP} vs H spectra of $SrIrO_3$(10 nm)/Py(20 nm) and Pt(5 nm)/Py(20 nm) bilayers at $f = 5.5$ GHz and input microwave power $P_{rf} = 90$ mW. The curves are offset for clarity. (c) The V_{SP} vs H spectra of $SrIrO_3$(10 nm)/Py(20 nm) at P_{rf} of 16, 28, 50, and 90 mW (green, purple, blue, and red curves, respectively). Inset: P_{rf} dependence of the corresponding V_{SP}. (d) Microwave frequency dependencies of FMR linewidth ΔH_{FMR} of a bare Py(20 nm) film, Pt(5 nm)/Py(20 nm), and $SrIrO_3$(10 nm)/Py(20 nm) samples.

contribution from anisotropic magnetoresistance associated with the metallic Py layer.[35,38] For the $SrIrO_3$(10 nm)/Py(20 nm) bilayer, the magnitude of V_{SP} reaches 82 μV, significantly larger than the 37.5 μV signal observed in the Pt(5 nm)/Py(20 nm) sample. Figure 4(c) shows the spin pumping spectra of the $SrIrO_3$(10 nm)/Py(20 nm) sample at different P_{rf} of 16, 28, 50, and 90 mW and $f = 5.5$ GHz. The inset shows the P_{rf} dependence of V_{SP}, demonstrating a linear microwave power dependence. Next, we perform frequency dependent FMR measurements on bare Py(20 nm), Pt(5 nm)/Py(20 nm), and $SrIrO_3$(10 nm)/Py(20 nm) samples to determine the FMR linewidth ΔH_{FMR} and the interfacial spin mixing conductance $g_{\uparrow\downarrow}$. In all cases, the measured ΔH_{FMR} follows a linear dependence on microwave frequency f as shown in Fig. 4(d). The obtained $g_{\uparrow\downarrow}$ at Pt/Py and $SrIrO_3$/Py interfaces are $(3.8 \pm 0.4) \times 10^{19}$ m^{-2} and $(1.1 \pm 0.1) \times 10^{19}$ m^{-2}, respectively. A reduced spin transfer efficiency at the $SrIrO_3$/Py interface in comparison with that from the Pt/Py interface could result from a reduced interfacial spin channel density in $SrIrO_3$/Py because of the much lower density of state in $SrIrO_3$ than Pt.

Finally, we provide a brief estimation on θ_{SH} of $SrIrO_3$ thin films based on the spin pumping results shown above. Due to the uncertainties involved in an accurate determination of local microwave field h_{rf} generated by the coplanar waveguide, here, we focus on obtaining a relative ratio between the spin Hall angle of $SrIrO_3$ (θ_{SIO}) and Pt (θ_{Pt}). In the spin pumping study, θ_{SH} could be determined by the following equation:[35,39]

$$\theta_{SH} = \frac{V_{SP}}{-wR\lambda_{SD}\tanh\left(\frac{t_{NM}}{2\lambda_{SD}}\right)J_s}, \quad (2)$$

where w is the sample width, R is the resistance of the bilayer sample, t_{NM} and λ_{SD} correspond to the film thickness and spin diffusion length of the spin detector, respectively. J_s denotes the magnitude of the spin current at the Py/spin-detector interface, which can be determined using spin mixing conductance $g_{\uparrow\downarrow}$, FMR linewidth ΔH_{FMR}, and h_{rf} with the relationship: $J_s \propto g_{\uparrow\downarrow}(\frac{h_{rf}}{\Delta H_{FMR}})^2$.[35,39] Based on the thickness dependent evolution of θ_{SIO}, the upper limit of λ_{SD} of $SrIrO_3$ is estimated to be $\sim$2 nm, in agreement with the experimentally reported value.[14] Here, we assume a similar λ_{SD} of Pt and $SrIrO_3$ with a magnitude much smaller than that of t_{NM},[14,40] yielding an insensitive term of $\tanh\left(\frac{t_{NM}}{2\lambda_{SD}}\right)$ in Eq. (2). By substituting those measured material parameters into the above equation, $|\theta_{SIO}|/|\theta_{Pt}|$ is estimated to be $\sim$3.5, qualitatively in agreement with the results obtained from the harmonic Hall method, confirming the exhibited large spin Hall effect of epitaxial $SrIrO_3$ thin films.

In summary, we reported a systematic investigation of spin–orbit coupling in epitaxial $SrIrO_3$ thin films. By measuring the harmonic Hall signals, a large spin-to-charge interconversion efficiency $|\theta_{SH}|$ up to $\sim$1.1 is determined at room temperature, which is further corroborated by ferromagnetic resonance-driven spin pumping measurements. Our results highlight the significant potential enabled by complex oxides in designing next-generation multifunctional spintronic devices for energy-favorable magnetic storage and logic devices.

This project was partially supported by the National Science Foundation under Grant No. 1639921, the Nanoelectronics Research Corporation (NERC), a wholly owned subsidiary of the Semiconductor Research Corporation (SRC), through Memory, Logic, and Logic in Memory Using Three Terminal Magnetic Tunnel Junctions, an SRC-NRI Nanoelectronics Research Initiative Center under Research Task ID 2700.001, the Center for Emergent Materials, an NSF MRSEC, under Grant No. DMR-1420451 (K.-Y.M.), and the U.S. Department of Energy (DOE) under Grant No. DE-SC0001304 (F.Y.Y).

REFERENCES

[1] J. E. Hirsch, Phys. Rev. Lett. **83**, 1834 (1999).
[2] J. Sinova, S. O. Valenzuela, J. Wunderlich, C. H. Back, and T. Jungwirth, Rev. Mod. Phys. **87**, 1213 (2015).
[3] Y. Otani, M. Shiraishi, A. Oiwa, E. Saitoh, and S. Murakami, Nat. Phys. **13**, 829 (2017).
[4] T. Tanaka, H. Kontani, M. Naito, T. Naito, D. S. Hirashima, K. Yamada, and J. Inoue, Phys. Rev. B **77**, 165117 (2008).
[5] M. Morota, Y. Niimi, K. Ohnishi, D. H. Wei, T. Tanaka, H. Kontani, T. Kimura, and Y. Otani, Phys. Rev. B **83**, 174405 (2011).
[6] L. Liu, C.-F. Pai, Y. Li, H. W. Tseng, D. C. Ralph, and R. A. Buhrman, Science **336**, 555 (2012).
[7] D. Qu, S. Y. Huang, B. F. Miao, S. X. Huang, and C. L. Chien, Phys. Rev. B **89**, 140407(R) (2014).
[8] X.-L. Qi and S.-C. Zhang, Rev. Mod. Phys. **83**, 1057 (2011).
[9] N. P. Armitage, E. J. Mele, and A. Vishwanath, Rev. Mod. Phys. **90**, 015001 (2018).
[10] M. König, S. Wiedmann, C. Brüne, A. Roth, H. Buhmann, L. W. Molenkamp, X.-L. Qi, and S.-C. Zhang, Science **318**, 766 (2007).
[11] K. Fujiwara, Y. Fukuma, J. Matsuno, H. Idzuchi, Y. Niimi, Y. Otani, and H. Takagi, Nat. Commun. **4**, 2893 (2013).
[12] D. J. Groenendijk, C. Autieri, J. Girovsky, M. C.Martinez-Velarte, N. Manca, G. Mattoni, A. M. R. V. L. Monteiro, N. Gauquelin, J. Verbeeck, A. F. Otte *et al.*, Phys. Rev. Lett. **119**, 256403 (2017).

[13]A. S. Patri, K. Hwang, H.-W. Lee, and Y. B. Kim, Sci. Rep. **8**, 8052 (2018).
[14]T. Nan, T. J. Anderson, J. Gibbons, K. Hwang, N. Campbell, H. Zhou, Y. Q. Dong, G. Y. Kim, N. Reynolds, X. J. Wang *et al.*, e-print arXiv:1808.06650.
[15]C. H. Du, R. Adur, H. L. Wang, A. J. Hauser, F. Y. Yang, and P. C. Hammel, Phys. Rev. Lett. **110**, 147204 (2013).
[16]A. J. Hauser, J. M. Lucy, H. L. Wang, J. R. Soliz, A. Holcomb, P. Morris, P. M. Woodward, and F. Y. Yang, Appl. Phys. Lett. **102**, 032403 (2013).
[17]Y. F. Nie, P. D. C. King, C. H. Kim, M. Uchida, H. I. Wei, B. D. Faeth, J. P. Ruf, J. P. C. Ruff, L. Xie, X. Pan *et al.*, Phys. Rev. Lett. **114**, 016401 (2015).
[18]D. Yi, C. L. Flint, P. P. Balakrishnan, K. Mahalingam, B. Urwin, A. Vailionis, A. T. N'Diaye, P. Shafer, E. Arenholz, Y. Choi *et al.*, Phys. Rev. Lett **119**, 077201 (2017).
[19]J. Liu, D. Kriegner, L. Horak, D. Puggioni, C. Rayan Serrao, R. Chen, D. Yi, C. Frontera, V. Holy, A. Vishwanath *et al.*, Phys. Rev. B **93**, 085118 (2016).
[20]K. Garello, I. M. Miron, C. O. Avci, F. Freimuth, Y. Mokrousov, S. Blügel, S. Auffret, O. Boulle, G. Gaudin, and P. Gambardella, Nat. Nanotechnol. **8**, 587 (2013).
[21]J. Kim, J. Sinha, M. Hayashi, M. Yamanouchi, S. Fukami, T. Suzuki, S. Mitani, and H. Ohno, Nat. Mater. **12**, 240 (2013).
[22]Y. Fan, P. Upadhyaya, X. Kou, M. Lang, S. Takei, Z. Wang, J. Tang, L. He, L.-T. Chang, M. Montazeri *et al.*, Nat. Mater. **13**, 699 (2014).
[23]T. Schulz, K. Lee, B. Krüger, R.-L. Conte, G. V. Karnad, K. Garcia, L. Vila, B. Ocker, D. Ravelosona, and M. Kläui, Phys. Rev. B **95**, 224409 (2017).
[24]U. H. Pia, K. W. Kim, J. Y. Bae, S. C. Lee, Y. J. Cho, K. S. Kim, and S. Seo, Appl. Phys. Lett. **97**, 162507 (2010).
[25]J. Finley and L. Liu, Phys. Rev. Appl. **6**, 054001 (2016).
[26]K. Ueda, M. Mann, C.-F. Pai, A. J. Tan, and G. S. D. Beach, Appl. Phys. Lett. **109**, 232403 (2016).
[27]N. Roschewsky, T. Matsumura, S. Cheema, F. Hellman, T. Kato, S. Iwata, and S. Salahuddin, Appl. Phys. Lett. **109**, 112403 (2016).
[28]R. Mishra, J. Yu, X. Qiu, M. Motapothula, T. Venkatesan, and H. Yang, Phys. Rev. Lett. **118**, 167201 (2017).
[29]K. J. Kim, S. K. Kim, Y. Hirata, S.-H. Oh, T. Tono, D.-H. Kim, T. Okuno, W. S. Ham, S. Kim, G. Go *et al.*, Nat. Mater. **16**, 1187 (2017).
[30]S. Emori, U. Bauer, S. M. Ahn, E. Martinez, and G. S. D. Beach, Nat. Mater. **12**, 611 (2013).
[31]C.-F. Pai, M. Mann, A. J. Tan, and G. S. D. Beach, Phys. Rev. B **93**, 144409 (2016).
[32]N. Nagaosa, J. Sinova, S. Onoda, A. H. MacDonald, and N. P. Ong, Rev. Mod. Phys. **82**, 1539 (2010).
[33]E. Saitoh, M. Ueda, H. Miyajima, and G. Tatara, Appl. Phys. Lett. **88**, 182509 (2006).
[34]B. Heinrich, C. Burrowes, E. Montoya, B. Kardasz, E. Girt, Y.-Y. Song, Y. Y. Sun, and M. Z. Wu, Phys. Rev. Lett. **107**, 066604 (2011).
[35]O. Mosendz, V. Vlaminck, J. E. Pearson, F. Y. Fradin, G. E. W. Bauer, S. D. Bader, and A. Hoffmann, Phys. Rev. B **82**, 214403 (2010).
[36]F. Y. Yang and P. C. Hammel, J. Phys. D: Appl. Phys. **51**, 253001 (2018).
[37]C. H. Du, H. L. Wang, Y. Pu, T. L. Meyer, P. M. Woodward, F. Y. Yang, and P. C. Hammel, Phys. Rev. Lett. **111**, 247202 (2013).
[38]W. Zhang, M. B. Jungfleisch, W. Jiang, J. E. Pearson, A. Hoffmann, F. Freimuth, and Y. Mokrousov, Phys. Rev. Lett. **113**, 196602 (2014).
[39]F. D. Czeschka, L. Dreher, M. S. Brandt, M. Weiler, M. Althammer, I.-M. Imort, G. Reiss, A. Thomas, W. Schoch, W. Limmer *et al.*, Phys. Rev. Lett. **107**, 046601 (2011).
[40]W. Zhang, V. Vlaminck, J. E. Pearson, R. Divan, S. D. Bader, and A. Hoffmann, Appl. Phys. Lett. **103**, 242414 (2013).